The Astrophysical Journal, 984:113 (10pp), 2025 May 9 https://doi.org/10.3847/1538-4357/adbf02

Reversals of Toroidal Magnetic Field in Local Shearing Box Simulations of Accretion Disk with a Hot Corona

Nishant K. Singh[1], Arunima Ajay[2,3], and S. R. Rajesh[2]
[1] Inter-University Centre for Astronomy & Astrophysics, Post Bag 4, Ganeshkhind, Pune 411 007, India; nishant@iucaa.in
[2] Department of Physics and Research Centre, S D College, University of Kerala, Kerala, India; arunima.ajay@sdcollege.in, srr@sdcollege.in
[3] Research Centre, University of Kerala, Kerala, India
Received 2024 October 18; revised 2025 February 19; accepted 2025 March 4; published 2025 May 2

Abstract

The presence of a hot corona above the accretion disk can have important consequences for the evolution of magnetic fields and the Shakura–Sunyaev viscosity parameter α in such a strongly coupled system. In this work, we have performed three-dimensional magnetohydrodynamical shearing-box numerical simulations of an accretion disk with a hot corona above the cool disk. Such a two-layer, piecewise isothermal system is vertically stratified under linear gravity, and initial conditions here include a strong azimuthal magnetic field with a ratio between the thermal and magnetic pressures being of order unity in the disk region. Instabilities in this magnetized system lead to the generation of turbulence, which, in turn, governs the further evolution of magnetic fields in a self-sustaining manner. Remarkably, the mean toroidal magnetic field undergoes a complete reversal in time by changing its sign, and it is predominantly confined within the disk. This is a rather unique class of evolution of the magnetic field that has not been reported earlier. Solutions of mean magnetic fields here are thus qualitatively different from the vertically migrating dynamo waves that are commonly seen in previous works, which model a single layer of an isothermal gas. Effective α is found to have values between 0.01 and 0.03. We have also make a comparison between models with Smagorinsky and explicit schemes for the kinematic viscosity (ν). In some cases with an explicit ν, we find a burst-like temporal behavior in α.

Unified Astronomy Thesaurus concepts: Stellar accretion disks (1579); Magnetic fields (994); Compact objects (288)

1. Introduction

A wide range of regimes of astrophysical MHD find their application in accretion disks around compact objects, which make these systems among the most explored in astrophysics for the past half century (J. E. Pringle 1981; S. A. Balbus & J. F. Hawley 1998; M. A. Abramowicz & P. C. Fragile 2013). The complex radiative features observed from these systems such as outbursts of dwarf novae and low-mass X-ray binaries (LMXBs; J. Smak 2000; B. Warner 2003; W. Lewin & M. van der Klis 2006; T. Bagnoli et al. 2015), aperiodic variabilities of X-ray binaries (W. Lewin & M. van der Klis 2006; R. A. Remillard & J. E. McClintock 2006; T. M. Belloni 2010), and active galactic nuclei (AGNs; A. J. Pica et al. 1988; U. Giveon et al. 1999; W. Ishibashi & T. J.-L. Courvoisier 2009; L. F. Sartori et al. 2018) indicate the existence of different limits of accretion. The temporal evolution of the radiative output of the accretion systems is attributed to different phases of inner sub-Keplerian accretion flows, such as advection-dominated accretion flows (R. Narayan & I. Yi 1994, 1995; M. A. Abramowicz et al. 1995; R. P. Fender et al. 2004; T. Belloni et al. 2005; R. A. Remillard & J. E. McClintock 2006; N. D. Kylafis & T. M. Belloni 2015), convection-dominated accretion flows (V. I. Igor & A. A. Marek 1999), adiabatic inflow–outflow solutions (R. D. Blandford & M. C. Begelman 1999), luminous hot accretion flows (F. Yuan 2001), jets (G. E. Romero et al. 2003; V. Bosch-Ramon et al. 2005; G. Piano et al. 2012), and coronas (E. M. de Gouveia Dal Pino & A. Lazarian 2005; E. M. de Gouveia Dal Pino et al. 2010; L. H. S. Kadowaki et al. 2015), fed by the outer standard cool Keplerian flow (I. D. Novikov & K. S. Thorne 1973; N. I. Shakura & R. A. Sunyaev 1973). Each of these phases of the accretion flow is characterized by an appropriate α parameter and cooling mechanisms (F. Yuan & R. Narayan 2014) determined by the mass-accretion rate.

From the spectral analysis of AGNs and X-ray transients, now it is fairly understood that the inner parts of the accretion disks around black holes and neutron stars are hot, optically thin, geometrically thick sub-Keplerian flows that are fueled by a much larger outer Keplerian flow domain, which is optically thick and geometrically thin disk. In the transition region, these two flow domains can coexist where a cool disk is embedded in a hot coronal flow (R. Wojaczyński et al. 2015; Y. Inoue et al. 2019; E. M. Gutiérrez et al. 2021). Such a structure raises the possibility of interaction of cool disk and hot corona. The radiative transport of the disk will be affected by the presence of hot corona and the global mass-energy exchange of the disk-corona system is modeled separately (F. Haardt & L. Maraschi 1991; F. Meyer et al. 2000; B. F. Liu et al. 2015; E. Meyer-Hofmeister et al. 2017; E. Qiao & B. F. Liu 2017). Moreover, the hydrodynamic and magnetic components of the viscous stress could be seriously modified in shear flow with such a strong vertical temperature jump. Therefore, it is important to analyze the temporal evolution of the local shearing patch corresponding to the disk-corona system and study the exchange of matter and magnetic energy.

The disk–corona interaction is fairly universal, and many phenomena associated with accretion systems can be reduced to such a topology. In the rest of the introduction, we briefly identify a few such cases. Interaction between the outer disk

and the radiation originating from the very inner part of the disk has been suggested in the context of outbursts in dwarf novae and X-ray transients (J. van Paradijs & J. E. McClintock 1995; J.-P. Lasota 1999). The thermoviscous instabilities causing these outbursts are modeled as influenced by this radiation exposure (J. van Paradijs & J. E. McClintock 1994; A. R. King & H. Ritter 1998; J.-P. Lasota 2001). Later, it was shown that (A. Rozanska & B. Czerny 1996; A. Maciołek-Niedźwiecki et al. 1997; A. Rózanska 1999) the heating of the outer disk from the top by the radiation originating from the inner part of the disk could create a hot corona above the cool disk. A transition region of sharp temperature gradient between the hot coronal layer of temperature of $\sim 10^9$ K and the disk of temperature of $\sim 10^4$ K is created. Such a configuration is shown to be unstable, which will spontaneously create hot coronal clouds above the cool disk. The interaction between the disk and the hot coronal patches could influence the evolution of the disk properties, particularly when they are magnetically coupled.

The physical mechanisms operating in accretion systems of different scales, such as LMXBs and quasars, are similar in nature. However, as the sources of the matter inflow are different, the very outer part of the disks themselves may have different topologies. In the case of LMXBs, the matter is supplied by Roche lobe overflow, and hence, the outer disk is mostly concentrated about the midplane of the disk. In the case of quasars or AGN's the matter is sourced by the hot wind from surrounding stars, and hence, the outer disk itself could have a relatively denser corona (B. F. Liu et al. 2015; E. Qiao & B. F. Liu 2017). Hence, in this context, the interaction between the disk and corona could also play a crucial role in the dynamic evolution of the accretion system.

Magnetorotational instability (MRI; S. Chandrasekhar 1960; S. A. Balbus & J. F. Hawley 1991) and the origin of turbulent viscosity in accretion disks have been discussed by numerous authors particularly with the types of initial magnetic field configurations such as an effective poloidal magnetic field (J. F. Hawley et al. 1995; X. N. Bai & J. M. Stone 2013; G. Salvesen et al. 2016a) and a zero net initial magnetic field or a weak toroidal field (A. Brandenburg et al. 1995; K. A. Miller & J. M. Stone 2000; S. W. Davis et al. 2010; J. B. Simon et al. 2012). The measured value of the α viscosity parameter in numerical experiments is smaller than by at least an order of magnitude of the expected value (A. R. King et al. 2007). Various modifications and generalizations, such as gravitational stratification, radially extended flow domain, and effect of radiative transport, have been explored by different authors (K. A. Miller & J. M. Stone 2000; S. Hirose et al. 2006; W. F. Winters et al. 2003). Numerical experiments on the vertically extended disk could generate magnetically dominated corona above a gas pressure-dominated disk (G. Salvesen et al. 2016a; L. H. S. Kadowaki et al. 2018) for a sufficiently strong initial magnetic field. Heating due to magnetic reconnection (B. F. Liu et al. 2003; C. Y. Huang et al. 2014) in this magnetically dominated corona could create a sharp temperature gradient across "the cool disk-hot corona system."

For all the plausible scenarios mentioned above, a vertically extended disk with temperature jump symmetrically above and below the midplane is a simple and faithful representation of the actual physical problem. On a global scale, the mass exchange between disk and corona, conduction from hot corona to cool disk, and the Comptonization of soft photons from disk by hot corona are the main interaction processes (F. Meyer et al. 2000; A. Różańska & B. Czerny 2000; R. A. Remillard & J. E. McClintock 2006; T. M. Belloni & S. E. Motta 2016). Whereas on a local scale, the interesting scenarios are the growth and evolution of magnetic field topology; hydrodynamic and magnetohydrodynamic instabilities and the effective viscous stress produced; and oscillations at the disk–corona interface.

We have studied a local three-dimensional magnetohydrodynamical numerical simulation using a shearing box approximation (J. F. Hawley et al. 1995) considering an initial stratified density distribution due to a linear gravity profile in the vertical direction and strong toroidal magnetic field. The disk-corona system is mimicked by imposing a temperature jump symmetrically in the vertical direction. This patch of the combined disk-corona system is allowed to evolve for several rotation times. The paper is organized as follows: In Section 2 we describe the setup of our model; in Section 3 we present the results; and in Section 4 we discuss our findings and conclusions.

2. Model and Numerical Setup

We numerically model a local patch of an accretion disk with a hot corona above by solving fully compressible hydromagnetic equations using the publicly available Pencil Code,[4] which is a high-order, finite-difference, modular, Message Passing Interface (MPI) code. Basic equations being solved may be expressed as

$$\frac{D\ln\rho}{Dt} = -\boldsymbol{\nabla}\cdot\boldsymbol{v}, \tag{1}$$

$$\frac{D\boldsymbol{v}}{Dt} = \boldsymbol{g} + \frac{1}{\rho}(\boldsymbol{J}\times\boldsymbol{B} - \boldsymbol{\nabla}p + \boldsymbol{\nabla}\cdot 2\nu\rho\mathsf{S}) - 2\Omega_0\hat{z}\times\boldsymbol{v} \tag{2}$$

$$\begin{aligned}\rho T\frac{Ds}{Dt} &= 2\rho\nu\mathsf{S}^2 + \mu_0\eta\boldsymbol{J}^2 - \boldsymbol{\nabla}\cdot\boldsymbol{F}_{\rm SGS}\\ &\quad -(\gamma-1)\rho c_p\frac{T-T_{\rm d,c}}{\tau_{\rm c}},\end{aligned} \tag{3}$$

$$\frac{\partial\boldsymbol{A}}{\partial t} = \boldsymbol{v}\times\boldsymbol{B} - \eta\mu_0\boldsymbol{J}, \tag{4}$$

where $\boldsymbol{v}$ is the velocity, $D/Dt = \partial/\partial t + \boldsymbol{v}\cdot\boldsymbol{\nabla}$ is the advective time derivative, $\boldsymbol{g}$ is the gravitational acceleration with a vertically linear profile, $\hat{z}$ is the unit vector along the vertical z-direction, $\mathsf{S}_{ij} = \frac{1}{2}(v_{i,j} + v_{j,i}) - \frac{1}{3}\delta_{ij}\boldsymbol{\nabla}\cdot\boldsymbol{v}$ is the traceless rate of strain tensor, where commas denote partial differentiation, $\nu =$ const is the kinematic viscosity, s is the specific entropy, ρ is the fluid density, p is the pressure, $\boldsymbol{A}$ is the magnetic vector potential, $\boldsymbol{B} = \boldsymbol{\nabla}\times\boldsymbol{A}$ is the magnetic field, $\boldsymbol{J} = \mu_0^{-1}\boldsymbol{\nabla}\times\boldsymbol{B}$ is the current density, $\eta =$ const is the magnetic diffusivity, μ_0 is the vacuum permeability, which is taken to be unity in our units, $\gamma = c_{\rm p}/c_{\rm v}$ is the ratio of specific heats at constant pressure and density, respectively, and T is the temperature.

In some cases we have also adopted a Smagorinsky model for viscosity with $\nu = \nu_{\rm S}$ where

$$\nu_{\rm S} = (C_k)\Delta^2\sqrt{\mathsf{S}^2}\,. \tag{5}$$

Here, C_k is the Smagorinsky constant and Δ is the filtering scale, which is chosen to be equal to the grid spacing; see, e.g.,

[4] http://github.com/pencil-code

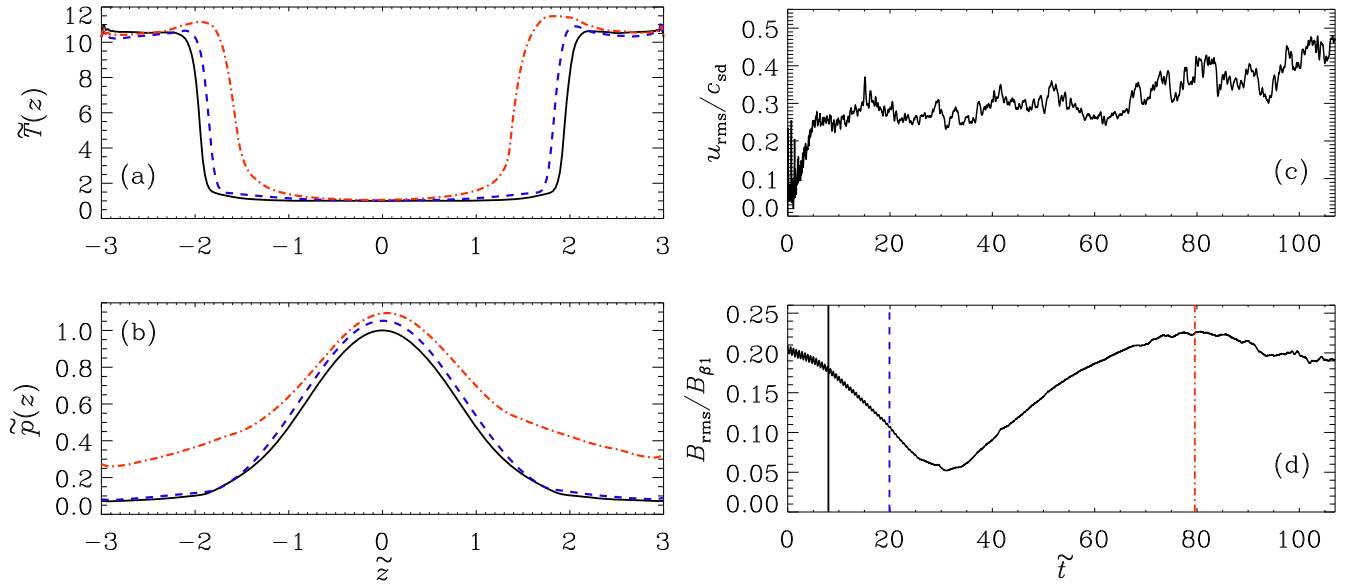

Figure 1. Profiles of (a) temperature and (b) pressure, as functions of normalized vertical coordinate $\tilde{z}$, with $\tilde{z} = 0$ being the midplane of the disk. Panels (c) and (d) display the temporal evolution of rms values of velocity deviations from the background shear flow and total magnetic field, respectively. Solid (black), dashed (blue), and dashed–dotted (red) curves in (a) and (b) show the profiles at three epochs in time that are marked by corresponding vertical lines in panel (d). These are shown from run A1sχ as listed in Table 1.

N. E. L. Haugen & A. Brandenburg (2006). We have used $C_k = 0.35$ in this work.

The last term in Equation (3) is a relaxation term that guarantees that the temperatures in the two subdomains, disk and corona, remain, on average, constant and equal to $T_{\rm d}$ (disk) and $T_{\rm c}$ (corona), respectively. In the present work, we applied the relaxation term only in the corona to maintain its temperature. This is preferable as it allows the flow to evolve more freely in the disk. In one of the simulations, A1sχ, we have used a subgrid-scale (SGS) diffusivity ($\chi_{\rm SGS}$), which acts on the fluctuations of the entropy about its horizontal average (P. J. K. Käpylä 2021). The SGS flux is given by

$$\boldsymbol{F}_{\rm SGS} = -\rho T \chi_{\rm SGS} \boldsymbol{\nabla} s' , \quad s' = s - \langle s \rangle_{xy}. \tag{6}$$

The angular velocity of the accretion disk at some arbitrary radius $R = R_0$ is denoted by Ω_0. In the rotating reference frame of the local Cartesian patch of the disk at R_0, the velocity field is in the toroidal y-direction with a linear shear profile:

$$\boldsymbol{V} = -q\Omega_0 x \hat{y}, \tag{7}$$

where $q = 3/2$ for a Keplerian disk, and $\hat{y}$ is the unit vector along the toroidal direction. The total velocity field is $v = \boldsymbol{V} + \boldsymbol{u}$, where $\boldsymbol{u}$ is the velocity deviation.

We assume an ideal fluid with an equation of state determining its pressure by $p = (c_{\rm p} - c_{\rm v})\rho T = \rho c_{\rm s}^2/\gamma$, where $c_{\rm s}$ is the adiabatic sound speed. Note that we have a piecewise isothermal setup where the disk (with sound speed $c_{\rm sd}$) and a hotter corona (with sound speed $c_{\rm su}$) are maintained at two different temperatures, as shown, for example, in Figure 1(a). The sharp jump in temperature or density at the disk–corona interface in the beginning is characterized by

$$\delta_0 = T_{\rm c}/T_{\rm d} = c_{\rm su}^2/c_{\rm sd}^2 = \rho_{i-}/\rho_{i+} , \tag{8}$$

where ρ_{i-} and ρ_{i+} are the densities just below and above the interface, respectively.

2.1. Scaling and Initial Conditions

In most of the simulations, we have a local cubical shearing box of side $6H$ (unless otherwise stated) and angular velocity Ω_0 with a temperature jump at $\pm 2H$ on either side of the midplane at $z = 0$, where $H = \Omega_0/c_{\rm sd}$. Initial density (or pressure) profiles of the medium, which is vertically stratified under linear gravity, are piecewise Gaussians in disk and corona. We choose a Gaussian profile along $\tilde{z}$ for the toroidal field $B_y(z)$ with an initial plasma parameter at the midplane being β_0. With $u_{\rm rms}$ being the rms value of the fluid velocity $\boldsymbol{u}$, we define dimensionless quantities as the plasma parameter as the initial ratio between the thermal and magnetic pressures, $\beta_0 = p/(B_y^2/2\mu_0)$, where β_0 is a constant in the disk region; Mach number ${\rm Ma} = u_{\rm rms}/c_{\rm sd}$; fluid Reynolds number ${\rm Re} = u_{\rm rms}H/\nu$; magnetic Reynolds number ${\rm Rm} = u_{\rm rms}H/\eta$; and shear parameter ${\rm Sh} = -q\Omega_0 H/c_{\rm sd}$.

We choose $\Omega_0 = 1$ and $c_{\rm sd} = 1$, giving $H = 1$. Time and length are scaled by rotation time $T = 2\pi/\Omega_0 = 2\pi$ and H, respectively. Density is scaled in units of initial midplane density ρ_0, and the magnetic field is scaled in units of $B_{\beta 1} = \sqrt{2\mu_0\rho_0}\, c_{\rm sd}$. The scaled magnetic field, time, and position are $\tilde{B}$, $\tilde{t}$, and $(\tilde{x}, \tilde{y}, \tilde{z})$, respectively.

2.2. Boundary Conditions

We have used shearing periodic boundary conditions in the radial direction (i.e., the x-coordinate) that reproduce the differential rotation through the angular displacement of the radial boundaries. The standard periodic boundary condition is applied in the angular direction (i.e., the y-coordinate). We study the interaction and evolution of the two preexisting flow domains, namely, the cold disk and the hot corona. In the vertical z-direction, we have used an impenetrable boundary condition such that $u_z = 0$ at the top and bottom boundaries of the domain. Thus, there is no outflow or mass loss from the domain. Although the matter is conserved in the combined system, an exchange of matter between the disk and corona

Table 1
Summary of Runs

Run	Domain	Grid	β_0	Ma	Re	Rm	Viscosity
A1sχ	$6H \times 6H \times 6H$	$256 \times 256 \times 256$	5.7	0.28	⋯	70.5	Smagorinsky
A2s	$6H \times 6H \times 6H$	$256 \times 256 \times 256$	5.7	0.31	⋯	78.2	Smagorinsky
A3e	$6H \times 6H \times 6H$	$256 \times 256 \times 256$	5.7	0.16	78	39	Explicit
B1e	$6H \times 6H \times 6H$	$128 \times 128 \times 128$	1.5	0.40	134	134	Explicit

Note. All runs have $H = 1$, Sh $= -1.5$, $q \equiv -S/\Omega_0 = 1.5$, and $\delta_0 = 10$.

components is possible. A vertical magnetic field boundary condition is applied at the two boundaries. Besides, the density is extrapolated, assuming a vertical hydrostatic equilibrium.

2.3. Diagnostics

In order to study the evolution of the system and the associated instabilities, we define the following averages. For a quantity $f = f(x, y, z, t)$, the volume average $\langle f \rangle_V$, and the planar average $\langle f \rangle$ are given by the expressions

$$\langle f \rangle_V = \frac{\int f dx dy dz}{\int dx dy dz}, \quad \langle f \rangle = \frac{\int f dx dy}{\int dx dy}. \tag{9}$$

The total stress tensor is given by

$$T_{xy}(z, t) = T_{xy}^{\rm Re}(z, t) + T_{xy}^{\rm Max}(z, t), \tag{10}$$

where $T_{xy}^{\rm Re}(z, t) = \langle \rho u_x u_y \rangle$ is the Reynolds stress, and $T_{xy}^{\rm Max}(z, t) = -\langle B_x B_y \rangle / \mu_0$ is the Maxwell stress. The z-dependent α viscosity parameter is defined as

$$\bar{\alpha}(z, t) = \frac{T_{xy}(z, t)}{\langle p \rangle}, \tag{11}$$

where $\langle p \rangle$ is the horizontally averaged gas pressure. By taking the rms value of $\overline{\alpha}$, let us define the time-varying viscosity parameter as $\alpha(t) = \sqrt{\langle \overline{\alpha}(z)^2 \rangle_z}$. The rms values of the fluid velocity and the total magnetic field are given by $u_{\rm rms} = \sqrt{\langle \boldsymbol{u}^2 \rangle_V}$ and $B_{\rm rms} = \sqrt{\langle \boldsymbol{B}^2 \rangle_V}$, respectively. Mean magnetic fields are defined with respect to the planar averages of normalized magnetic fields as $\overline{B}_x(z, t) = \langle \widetilde{B}_x \rangle$ and $\overline{B}_y(z, t) = \langle \widetilde{B}_y \rangle$.

3. Results

We present our results from the simulations that are listed in Table 1.

3.1. A1sχ Model

This is a large eddy simulation (LES) with a Smagorinsky viscosity in a shearing box. It covers about ∼110 orbits. With $\beta_0 = 5.7$, the initially imposed toroidal magnetic field is strong in this case, and therefore, the Parker-Rayleigh–Taylor instability (PRTI) is expected to be operational (L. H. S. Kadowaki et al. 2018). Run A2s, as listed in Table 1, has a slightly larger Rm, but is otherwise similar to the A1sχ model. Findings from these two runs are quite similar, so below we present results from run A1sχ.

3.1.1. Vertical Structure of the Disk-corona System

Figure 1 shows the vertical profile of the thermodynamic variables and the time evolution of volume average based rms strengths of the fluid velocity ($u_{\rm rms}$) and total magnetic field ($B_{\rm rms}$) from the combined disk-corona system. As may be seen from Figure 1(a), a temperature jump, with a corresponding drop in the density (not shown), in the corona by factor 10 compared with the disk is maintained during the simulation. The relaxation term in the entropy equation is applied only for the layers with $|\tilde{z}| \geqslant 2$. As time passes, we do observe a gradual drift of the transition layer in such a way that the extent of the corona increases. This is expected due to heating in the system by magnetic reconnection.

Thus, we have a piecewise isothermal domain where a cold disk is embedded between the coronal envelope of higher temperature. The system is vertically stratified under linear gravity, which leads to correspondingly piecewise Gaussian profiles for pressure as well as density in the disk and corona; see Figure 1(b) where $\tilde{z} = 0$ is the midplane of the disk, and the pressure is continuous across the interface. In Section 3.1.3, we also show the vertical profile of the density in code units. Note that due to the impenetrable boundary condition being adopted in this work, there is no mass loss from the system.

Turbulence is quickly produced within a few rotation times due to the magnetic field. The flow is subsonic, and $u_{\rm rms}$ shows a saturation after about 20 rotation times. The simulation starts with an initial toroidal magnetic field B_y which is Gaussian in structure with $\beta_0 = 5.7$. Figure 1(d) shows that $B_{\rm rms}$ decays in the beginning, and after about 30 rotation times, it starts to grow. This growing phase is linked to the reversal of the toroidal magnetic field; see the paragraph below for a discussion on the reversal of $\overline{B}_y$. Both the magnetic field and the turbulence are maintained self-consistently in this system.

3.1.2. Reversal of the Toroidal Magnetic Field ($\overline{B}_y$)

Figure 2 shows the spacetime diagrams of the horizontally averaged mean magnetic fields, $\overline{B}_y$ (left, top) and $\overline{B}_x$ (left, bottom), which are normalized by $B_{\beta 1}$ defined earlier. Remarkably, the mean toroidal magnetic field undergoes a complete reversal in time by changing its sign, and it is predominantly confined within the disk. This is a rather unique class of evolution of the magnetic field that has not been reported earlier; see the spacetime diagrams in Figure 2 and in a number of other cases discussed below. The x-component of the mean magnetic field is mostly confined in the coronal regions, and it is generated by the MHD instabilities in this system.

Vertically migrating dynamo waves are commonly seen in a number of previous works that typically model an isothermal disk (A. Brandenburg et al. 1995; J. B. Simon et al. 2012;

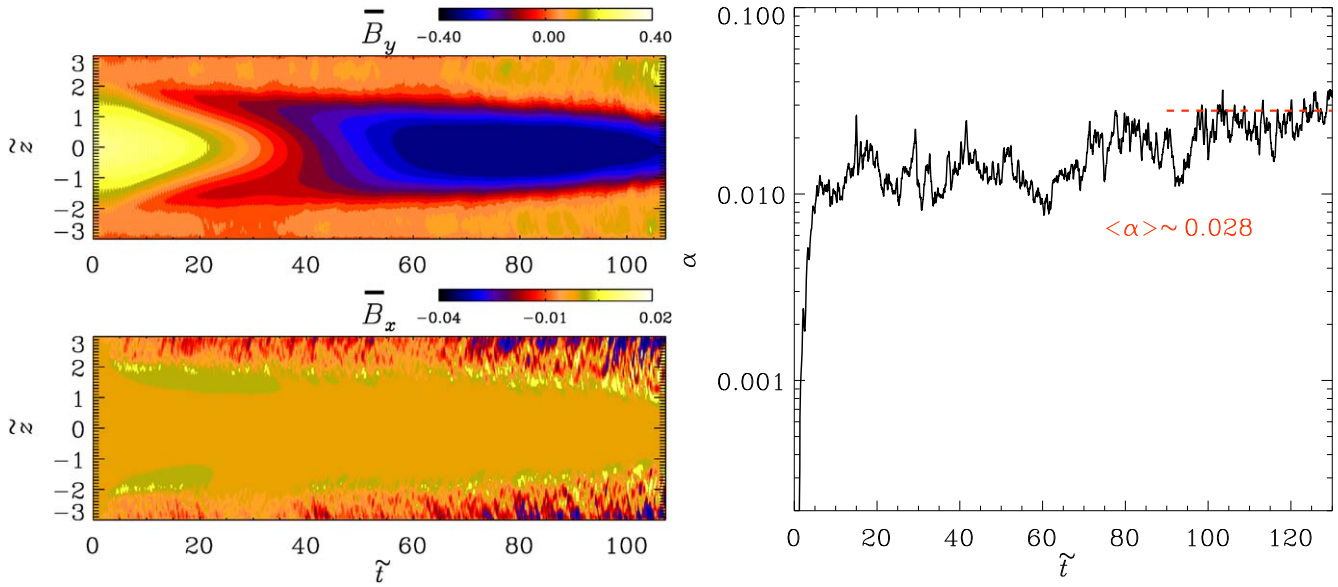

Figure 2. Left: spacetime diagrams of horizontally averaged mean magnetic fields, $\overline{B}_y$ (top) and $\overline{B}_x$ (bottom), which are normalized by $B_{\beta 1}$. Right: temporal behavior of the viscosity parameter α. These are shown from run A1sχ as listed in Table 1.

G. Salvesen et al. 2016b; L. H. S. Kadowaki et al. 2018). The reversal of the toroidal magnetic field that we find in this work is quite intriguing. Unlike magnetic field solutions in isothermal boxes considered in earlier works, we find here that the first moments of the magnetic fields, $\overline{B}_x$ and $\overline{B}_y$, are spatially separated. This is caused by the hot corona above the disk.

Figure 3 shows the vertical profile of the density in code units from run A3e as listed in Table 1.

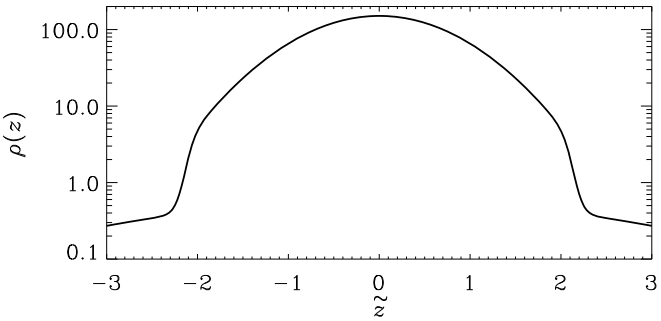

Figure 3. Vertical profile of the density in code units from run A3e as listed in Table 1.

3.1.3. Vertical Magnetic Fields

In Figure 4, we show profiles of the unaveraged vertical magnetic fields from the snapshots taken at different times where we chose to display the structure from the $y = 0$ plane. These fields are produced by the action of buoyancy effects in such stratified systems, which are expected to host instabilities such as MRI and PRTI. As is evident from Figure 4, B_z is predominantly confined in the low-density coronal regions where it appears to be of small scale in nature, and its strength increases in time.

3.1.4. Viscosity Parameter (α)

Time evolution of the Shakura–Sunyaev (SS) viscosity parameter (α) as defined below Equation (11) is shown in the right panel of Figure 2. We find that α saturates with a mean value of $\sim$0.03 after about 50 rotation times. This is about 10 times larger compared with the value of α obtained for simulations of zero outflow boundary conditions with initial vertical magnetic field of $\beta_0 \sim 0.1$ (A. Brandenburg et al. 1995) and initial zero net magnetic field/initial toroidal magnetic field of $\beta_0 \sim 100$ (J. M. Stone et al. 1996). Saturated values of α in this work are close to those seen in simulations of outflow boundary condition with zero net initial magnetic field/initial toroidal magnetic field of $\beta_0 \sim 10$ (K. A. Miller & J. M. Stone 2000) and initial toroidal magnetic field of $\beta_0 \sim 1$ (L. H. S. Kadowaki et al. 2018).

3.1.5. Comparison between Models with Different Numerical Schemes for Kinematic Viscosity (ν)

In order to test how sensitive our results are to the numerical schemes adopted for ν, we perform another set of simulations with explicit kinematic viscosity. One such run, called A3e in Table 1, is presented in this work; see the Appendix where we include results from this run with explicit ν.

Note that this has a smaller Rm (and Re = 78) compared with the A1sχ model, with the Smagorinsky viscosity discussed above in Section 3.1. Broad conclusions from models with these two different numerical schemes for ν are the same, i.e., the toroidal magnetic field undergoes a complete reversal as discussed in Section 3.1. Further discussion on this is deferred to the Appendix.

3.1.6. Models with $\beta_0 = 1.5$ and Oppositely Directed Initial Magnetic Field Configurations

Here, we present results from two lower resolution runs, B1e (listed in Table 1) and B1eN, which is identical to run B1e, except that the initial B_y in this case has the opposite sign. We have used explicit ν in both these cases where we test the robustness of our findings discussed above on the field reversals. In Figures 5 and 6, we show the spacetime diagrams of mean magnetic fields, $\overline{B}_x$ and $\overline{B}_y$, as well as

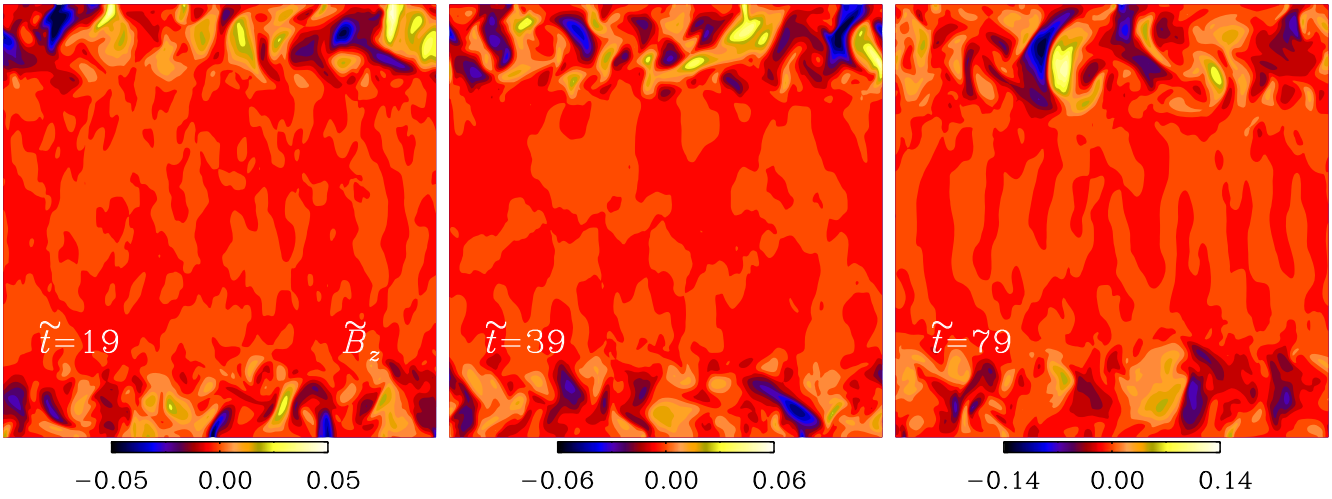

Figure 4. Three snapshots of the normalized vertical magnetic field ($\widetilde{B}_z$) from the $y = 0$ plane from run A1sχ; see Table 1 and Figure 2.

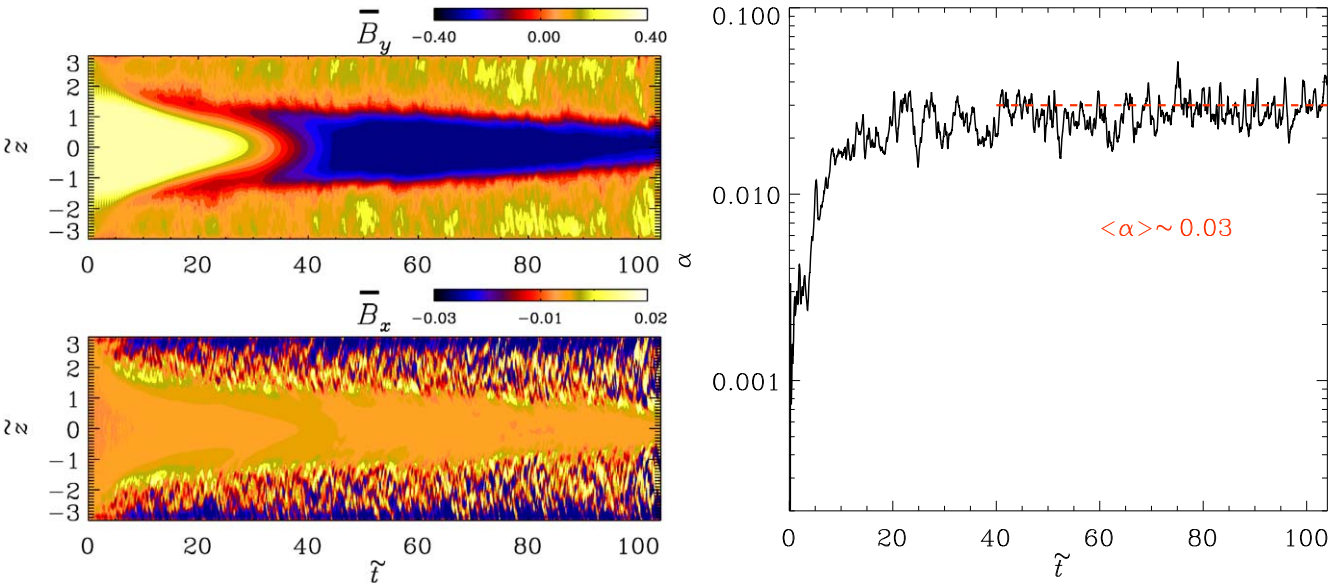

Figure 5. Same as Figure 2 but from run B1e listed in Table 1.

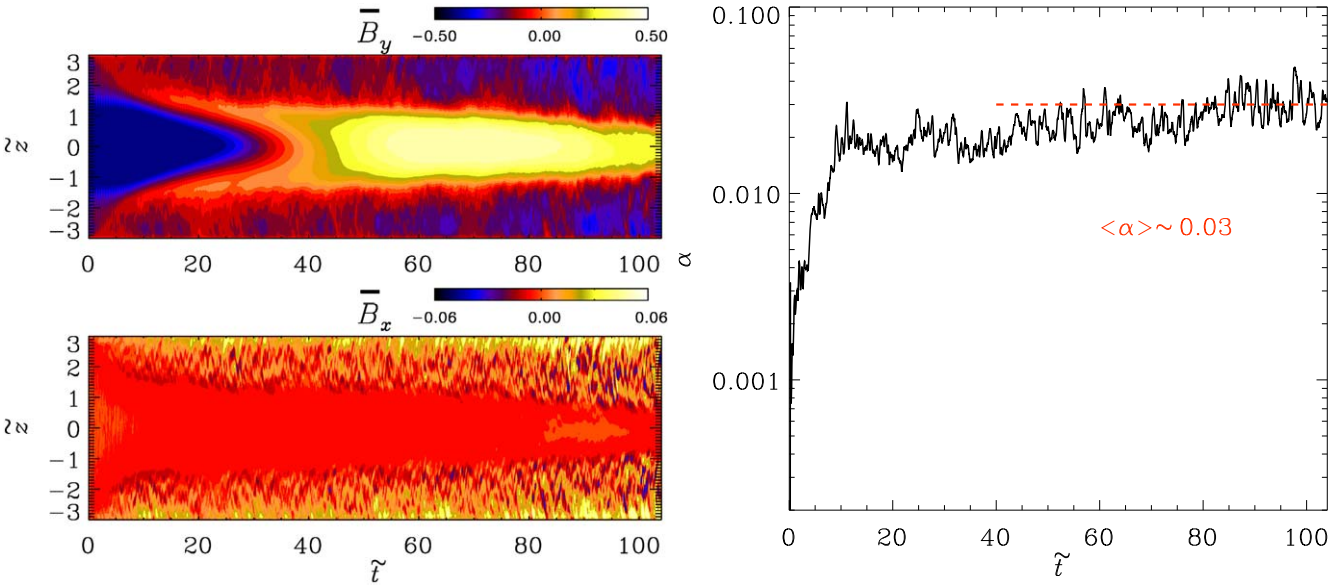

Figure 6. Same as Figure 2 but from run "B1eN" (not listed in Table 1), which is identical to run B1e of Table 1, except that the initial B_y in this case has the opposite sign.

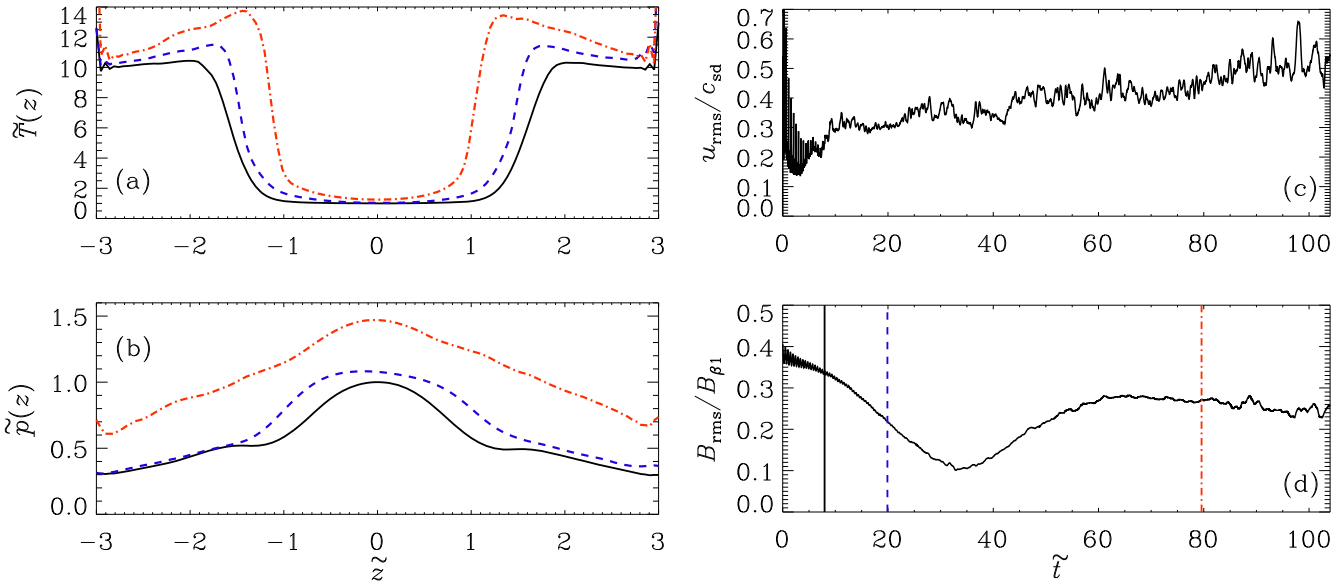

Figure 7. Same as Figure 1 but from the lower resolution run "B1eN"; see the caption of Figure 6.

the time evolution of the SS viscosity parameter α. Mean toroidal field $\overline{B}_y$ undergoes a complete reversal in time by changing its sign in both these cases, and the SS viscosity parameter α saturates to a mean value of $\sim$0.03 after about 30 rotation times.

As may be seen from Figure 7(a), there is a gradual drift of the disk–corona interface also in these cases such that the extent of hotter corona slowly increases. Recall that the relaxation term, as discussed in Section 2, to maintain the corona of higher (lower) temperature (density) is applied only in layers with $|\tilde{z}| \geqslant 2$. Figure 7(c) shows the instabilities in the magnetized disk drive turbulence, which, in turn, governs the evolution of the magnetic field in a self-sustaining manner. Ohmic heating due to magnetic reconnection of small-scale loop-like structures, which are prominent in low-density coronal regions, is likely the cause for further heating of corona. This is expected to play a crucial role in the formation of corona in the magnetized accretion disks.

4. Discussion and Conclusions

The geometrically thin gas pressure-dominated accretion disk cannot completely explain the phenomenology of accretion disks around compact objects such as X-ray Binaries and AGNs (B. Mishra et al. 2020). Thermoviscous instabilities and high-energy spectral characteristics from these sources indicate that hot geometrically thick and magnetized component of accretion flow is also present (M. C. Begelman & J. E. Pringle 2007; E. Gaburov et al. 2012). Magnetic energy dissipation is the main internal mechanism of heating of the disk except the irradiation by the very inner part of the accretion disk. There are several attempts to explain the self-sustained generation of large-scale magnetic fields in accretion around compact objects. It is argued that even if the system starts with a very weak magnetic field, strong toroidal magnetic field could be sustained in a later phase (T. Kudoh et al. 2002; M. E. Pessah & D. Psaltis 2005) driven by MRI (K. A. Miller & J. M. Stone 2000; L. H. S. Kadowaki et al. 2015; M. C. Begelman et al. 2015). In our work, we choose such an initial organized toroidal magnetic field (M. C. Begelman & J. E. Pringle 2007), which is superposed on a preexisting cold disk-hot corona, as discussed in the Introduction.

The main results of this work can be summarized as follows:

(a) The cold disk hot corona vertical temperature profile is stable: in all the simulations, the symmetric step profile of the temperature as a function of vertical coordinate is maintained. The results are independent of Smagorinsky or an explicit scheme for the kinematic viscosity.

(b) Instabilities in the magnetized disk drive turbulence, which, in turn, governs the evolution of a magnetic field in a self-sustaining manner.

(c) The large-scale toroidal magnetic field is largely confined to the cold disk region: contrary to the general belief, in the cold disk-hot corona system, the large-scale toroidal magnetic field is strong in the disk region and weakens in the corona region. It is found that the system suppresses the magnetic buoyant force, confining the large-scale toroidal magnetic field in the disk region.

(d) Remarkably, the mean toroidal magnetic field undergoes a complete reversal in time by changing its sign, and it is predominantly confined within the disk. This is a rather unique class of evolution of the magnetic field that has not been reported earlier. The toroidal magnetic field thus shows an aperiodic field reversal.

Vertically extended shearing box simulations in other works where an isothermal gas is modeled, one typically finds dynamo waves, i.e., a butterfly pattern for mean fields that show quasiperiodicity over timescales on the order of 10 rotation times. In our case, with a piecewise isothermal disk-corona system, we find that the toroidal fields reverses over a timescale of the order of 50 rotation times, and the commonly seen butterfly pattern of the dynamo wave is absent.

(e) The saturated value of the SS viscosity parameter α is about 0.03 for several tens of rotation times. This is in conformity with most of the shearing box simulations of a magnetized accretion disk. The Maxwell stress is found to be stronger than the Reynolds stress, and it largely contributes to α.

Astrophysical systems, such as stars, galaxies, accretion disks, etc., are highly turbulent with very large Reynolds numbers where typical values in disks are estimated to be of order 10^{11}. Numerical modeling of astrophysical objects at such large values seems formidable even in the foreseeable future. Even the most advanced and high-resolution simulations employing explicit diffusion schemes model these objects with Reynolds numbers not exceeding values of order 10^3. One nevertheless hopes that these modest numbers are still able to capture the essence of various physical mechanisms, which are expected to reach an asymptotic regime where the mechanisms become independent of control parameters. These are recognized as challenging problems in the community. This emphasizes the need for advanced subgrid-scale analytical models, which could allow us to study some global properties of these systems using modest numbers of grid points. LES models have been useful in these efforts, and therefore, we have also performed LES models in this work to confirm if our broad conclusions listed above hold.

Thermal Comptonization (S. L. Shapiro et al. 1976; R. A. Sunayev & L. G. Titarchuk 1980) in the hot and low dense corona is generally invoked to explain the high-energy emission. Apart from the continuous corona, distinct active regions of coronal clouds above the disk are also suggested in this context (F. Haardt et al. 1994). In a magnetically coupled disk-corona system, the interaction could cause a further increase in the coronal temperature (H. Kuneida et al. 1990; A. A. Zdziarski et al. 1990; F. Haardt & L. Maraschi 1991; A. Merloniw & A. C. Fabian 2001). The amplification of the seed magnetic field in the disk by differential rotation and convection is generally balanced by microscopic diffusivities. In a gravitationally stratified gas, a horizontal magnetic field can trigger unstable modes, leading to Parker instability (E. N. Parker 1958, 1966). In an isothermal setup, if the magnetic field cannot dissipate at the rate of amplification, then the magnetic field could emerge from the disk to the coronal region due to buoyancy, and magnetic loops could dissipate in the coronal region (A. Galeev et al. 1979).

Differentially rotating systems such as disk galaxies show magnetic field reversals while moving radially (J. P. Vallee 1996; P. Frick et al. 2001; C. L. Van Eck et al. 2011). Mechanisms such as the turbulent dynamo effect and stellar feedback are involved in understanding the evolution of magnetic fields in these systems (H. Kotarba et al. 2009; A. Brandenburg 2015). Fully isothermal, shearing box simulations to model accretion disks reveal a butterfly pattern where the dynamo wave leads to a quasiperiodicity in mean magnetic fields with a period of about 10 rotation times (A. Brandenburg et al. 1995; L. H. S. Kadowaki et al. 2015; G. Salvesen et al. 2016b; L. H. S. Kadowaki et al. 2018). Whereas in our two-layer system of cool disk and a hot corona, the quasiperiodicity of mean fields as found in earlier works is absent. Instead, the mean toroidal magnetic field undergoes a complete reversal over a timescale of about 50 rotations by changing its sign, and it is predominantly confined within the disk.

Interaction of a hot corona on top of a cool disk was invoked in the context of the so-called slab model to explain thermal Comptonized X-rays from the disk (J. B. Dove et al. 1997a, 1997b). Observations in black hole binaries and AGNs show that the fraction of total energy dissipated in corona is very large (F. Haardt & L. Maraschi 1991; P. O. Petrucci et al. 2018). Magnetically supported steady-state accretion disk-corona models with active MRI (D. Gronkiewicz & A. Różańska 2019) also suggest that an appreciable amount of energy release could happen in the corona region.

The global simulations on accretion disk vary from thick disk/accretion torus (J. F. Hawley 2001; M. Machida et al. 2000) to the vertically extended cylindrical disk with a Keplerian shear profile (J. F. Hawley 2000; P. J. Armitage et al. 2001; K. A. Sorathia et al. 2012). The cylindrical disk simulations are useful to study the global evolution of magnetically driven turbulence and, in a sense, are the natural extension of the local rotating shearing box simulations. Global simulations with net vertical magnetic field have shown an outflow component (T. K. Suzuki & S.-I. Inutsuka 2014; O. Gressel et al. 2015), whereas a net poloidal component is known to be effective in accretion below the wind region similar to our case. Simulations on global magnetized accretion disk suggest that the system can have accretion via corona and outflow from midplane (K. Beckwith et al. 2009; Z. Zhu & J. M. Stone 2018), which is consistent with our results.

As noted above, $\overline{B}_y$ is largely confined to the disk region due to the presence of a hot corona above. Whereas $\overline{B}_x$, and also B_z, are prominent in the corona; see Section 3.1. We envisage that ohmic heating due to magnetic reconnection of smaller scale field structures will be more efficient in the coronal region, producing thus an excess heat which may heat-up the disk. The corona thus "advances" toward the disk, swallowing the matter from the disk to facilitate more efficient accretion of the matter. This particular situation could create a scenario of accretion via corona.

Acknowledgments

This work used the High Performance Computing Facility of IUCAA, Pune (http://hpc.iucaa.in). A.A. thanks the Council for Scientific and Industrial Research, Government of India, for the research fellowship. S.R.R. thanks IUCAA, Pune, for the Visiting Associateship Program. We thank the referee for the useful comments.

Appendix
Field Reversals in Runs with Explicit Kinematic Viscosity

Here, we show results from run A3e listed in Table 1, where we adopt an explicit diffusion scheme for the kinematic viscosity (ν), to demonstrate that the results presented in Section 3 are robust. In Figure 8, we show the vertical profiles and the temporal evolution of the thermodynamic variables. Also shown are the time dependence of $u_{\rm rms}$ and $B_{\rm rms}$. The sharp transition between the cool disk and the hot corona by the relaxation term in Equation (3) is better maintained in time in this case. Recall that, just like the other cases discussed in this work, the run begins with a toroidal field B_y with a Gaussian profile along $\tilde{z}$ such that the initial $\beta_0 = 5.7$ is constant within the disk.

From Figures 8(c) and (d), we note that while the $B_{\rm rms}$ evolves smoothly as in Figure 1 for the A1sχ model, $u_{\rm rms}$ shows an outburst-like activity in time. This leads to an interesting, burst-like temporal evolution of the SS viscosity parameter α, as shown in the right panel of Figure 9. The peak value of the α exceeds the value 0.01, which is consistent with our findings as presented in Section 3, and also with the values reported in some other works discussed before.

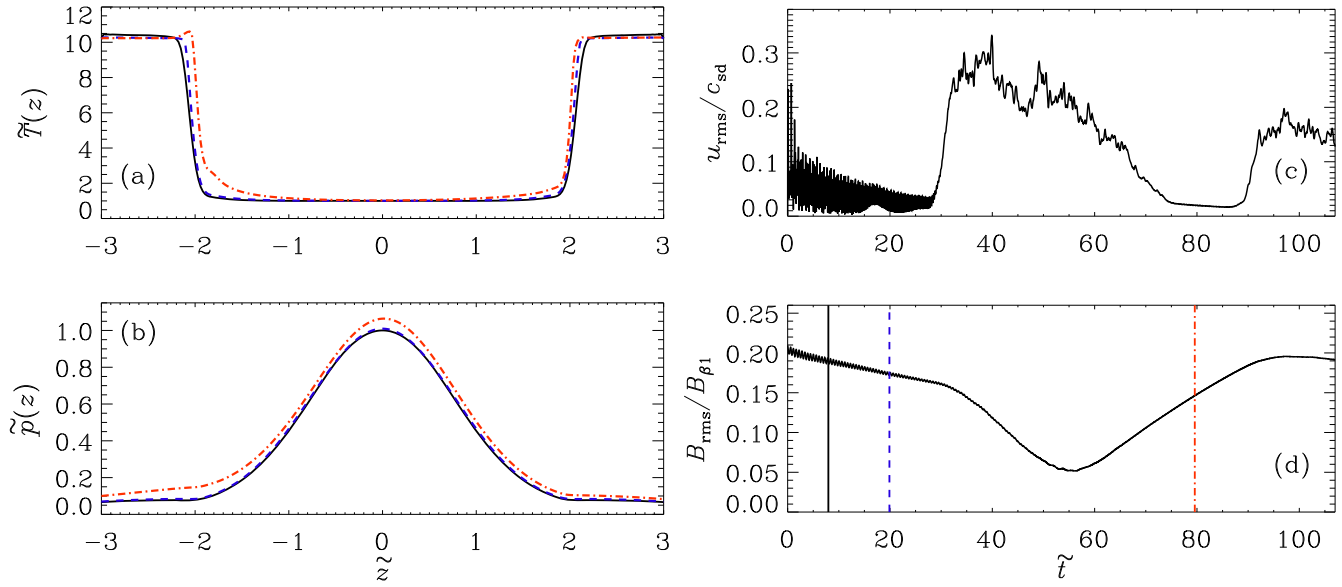

Figure 8. Same as Figure 1 but from run A3e as listed in Table 1.

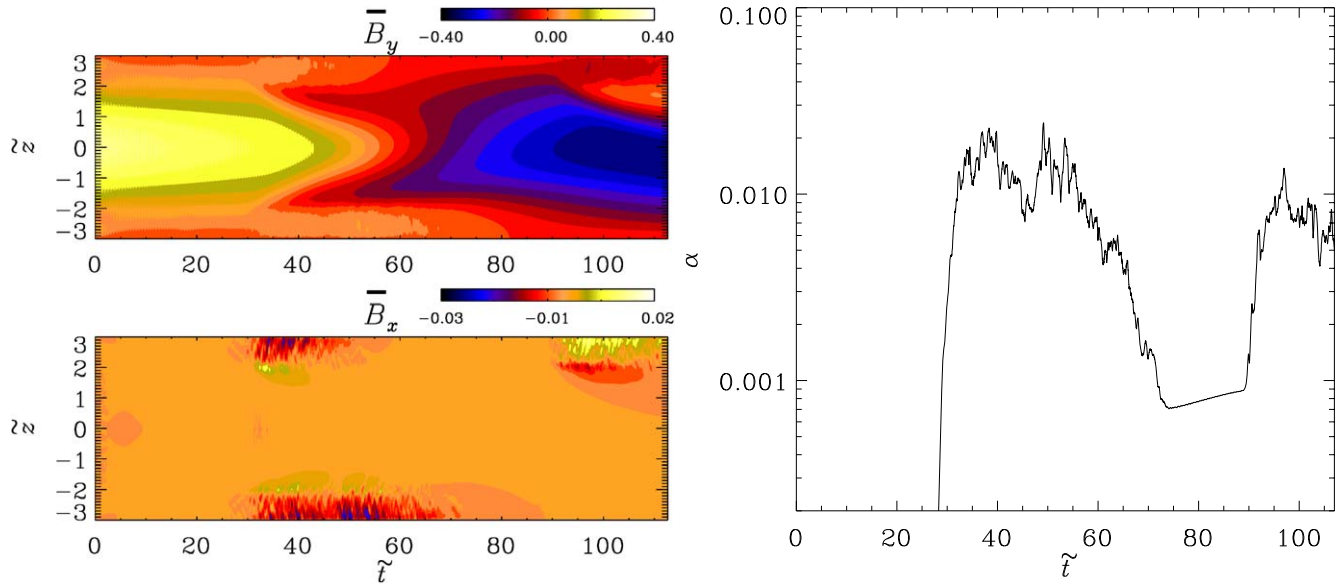

Figure 9. Same as Figure 2 but from run A3e as listed in Table 1.

Spacetime diagrams of mean magnetic fields, $\overline{B}_x$ and $\overline{B}_y$, as shown in Figure 9, reveal the reversal of the toroidal component, which is strongest in the disk region, whereas $\overline{B}_x$ is strong in the coronal regions. This is consistent with the results presented in Section 3 where a number of cases with Smagorinsky scheme for ν also show a similar pattern. The results presented in this work are thus independent of the numerical schemes for kinematic viscosity. Burst-like behavior of the SS viscosity parameter α in time may have interesting consequences for accretion patterns and may help us better understand the observations. In future work, we will focus more on this by performing simulations at larger Reynolds numbers.

ORCID iDs

Nishant K. Singh https://orcid.org/0000-0001-6097-688X
S. R. Rajesh https://orcid.org/0000-0002-7717-0521

References

Abramowicz, M. A., Chen, X., Kato, S., Lasota, J.-P., & Regev, O. 1995, ApJL, 438, L37
Abramowicz, M. A., & Fragile, P. C. 2013, LRR, 16, 1
Armitage, P. J., Reynolds, C. S., & Chiang, J. 2001, ApJ, 548, 868
Bagnoli, T., in 't Zand, J. J. M., D'Angelo, C. R., & Galloway, D. K. MNRAS 2015, 449, 268
Bai, X. N., & Stone, J. M. 2013, ApJ, 767, 30
Balbus, S. A., & Hawley, J. F. 1991, ApJ, 376, 214
Balbus, S. A., & Hawley, J. F. 1998, RvMP, 70, 1
Beckwith, K., Hawley, J. F., & Krolik, J. H. 2009, ApJ, 707, 428
Begelman, M. C., Armitage, P. J., & Reynolds, C. S. 2015, ApJ, 809, 118
Begelman, M. C., & Pringle, J. E. 2007, MNRAS, 375, 1070
Belloni, T., Homan, J., Casella, P., et al. 2005, A&A, 440, 207
Belloni, T. M. 2010, The Jet Paradigm: Lecture Notes in Physics (Berlin: Springer)
Belloni, T. M., & Motta, S. E. 2016, Astrophysics of Black Holes, 440 (Berlin: Springer), 61
Blandford, R. D., & Begelman, M. C. 1999, MNRAS, 303, L1
Bosch-Ramon, V., Aharonian, F. A., & Paredes, J. M. 2005, A&A, 432, 609

Brandenburg, A. 2015, in Magnetic Fields in Diffuse Media: Astrophysics and Space Science Library, ed. A. Lazarian, E. M. de Gouveia Dal Pino, & C. Melioli, 407 (Berlin: Springer), 529
Brandenburg, A., Nordlund, A., Stein, R. F., & Torkelsson, U. 1995, ApJ, 446, 741
Chandrasekhar, S. 1960, PNAS, 46, 253
Davis, S. W., Stone, J. M., & Pessah, M. E. 2010, ApJ, 713, 52
de Gouveia Dal Pino, E. M., & Lazarian, A. 2005, A&A, 441, 845
de Gouveia Dal Pino, E. M., Piovezan, P. P., & Kadowaki, L. H. S. 2010, A&A, 518, 5
Dove, J. B., Wilms, J., & Begelman, M. 1997a, ApJ, 487, 747
Dove, J. B., Wilms, J., Maisack, M., & Begelman, M. 1997b, ApJ, 487, 759
Fender, R. P., Belloni, T. M., & Gallo, E. 2004, MNRAS, 355, 1105
Frick, P., Stepanov, R., Shukurov, A., & Sokoloff, D. 2001, MNRAS, 325, 649
Gaburov, E., Johansen, A., & Levin, Y. 2012, ApJ, 758, 103
Galeev, A., Rosner, R., & Vaiana, G. S. 1979, ApJ, 229, 318
Giveon, U., Maoz, D., Kaspi, S., Netzer, H., & Smith, P. 1999, MNRAS, 306, 637
Gressel, O., Turner, N. J., Nelson, R. P., & McNally, C. P. 2015, ApJ, 801, 84
Gronkiewicz, D., & Różańska, A. 2019, A&A, 633, A35
Gutiérrez, E. M., Vieyro, F. L., & Romero, G. E. 2021, A&A, 649, A87
Haardt, F., & Maraschi, L. 1991, ApJ, 380, L51
Haardt, F., Maraschi, L., & Ghisellini, G. 1994, ApJ, 432, L95
Haugen, N. E. L., & Brandenburg, A. 2006, PhFl, 18, 075106
Hawley, J. F. 2000, ApJ, 528, 462
Hawley, J. F. 2001, ApJ, 554, 534
Hawley, J. F., Gammie, C. F., & Balbus, S. A. 1995, ApJ, 440, 742
Hirose, S., Krolik, J. H., & Stone, J. M. 2006, ApJ, 640, 901
Huang, C. Y., Wu, Q., & Wang, D.X. 2014, MNRAS, 440, 965
Igor, V. I., & Marek, A. A. 1999, MNRAS, 303, 309
Inoue, Y., Khangulyan, D., Inoue, S., & Doi, A. 2019, ApJ, 880, 40
Ishibashi, W., & Courvoisier, T. J.-L. 2009, A&A, 504, 61
Kadowaki, L. H. S., de Gouveia Dal Pino, E. M., & Singh, C. B. 2015, ApJ, 802, 113
Kadowaki, L. H. S., de Gouveia Dal Pino, E. M., & Stone, J. M. 2018, ApJ, 864, 52
Käpylä, P. J. K. 2021, A&A, 655, A78
King, A. R., Pringle, J. E., & Livio 2007, MNRAS, 376, 1740
King, A. R., & Ritter, H. 1998, MNRAS, 293, L42
Kotarba, H., Lesch, H., Dolag, K., et al. 2009, MNRAS, 397, 733
Kudoh, T., Matsumoto, R., & Shibata, K. 2002, PASJ, 54, 121
Kuneida, H., Turner, T. J., Awaki, H., et al. 1990, Natur, 345, 786
Kylafis, N. D., & Belloni, T. M. 2015, A&A, 574, A133
Lasota, J.-P. 1999, in Proc. of the Disk-Instability Workshop, 25 Years of the Disk Instability Model, ed. S. Mineshige & J. C. Wheeler (Tokyo: Universal Academy), 191
Lasota, J.-P. 2001, NewAR, 45, 449
Lewin, W., & van der Klis, M. 2006, Compact Stellar X-Ray Sources (Cambridge: Cambridge Univ. Press)
Liu, B. F., Mineshige, S., & Ohsuga, K. 2003, ApJ, 587, 571
Liu, B. F., Taam, R., Qiao, E., et al. 2015, ApJ, 806, 223
Machida, M., Hayashi, M. R., & Matsumoto, R. 2000, ApJ, 532, L67
Maciołek-Niedźwiecki, A., Krolik, J. H., Zdziarski, A. A., et al. 1997, ApJ, 483, 111
Merloniw, A., & Fabian, A. C. 2001, MNRAS, 321, 549
Meyer, F., Liu, B. F., & Meyer-Hofmeister, E. 2000, A&A, 361, 175
Meyer-Hofmeister, E., Liu, B. F., & Qiao, E. 2017, A&A, 607, A94
Miller, K. A., & Stone, J. M. 2000, ApJ, 534, 398
Mishra, B., Begelman, M. C., Armitage, P. J., & Simon, J. B. 2020, MNRAS, 492, 1855
Narayan, R., & Yi, I. 1994, ApJL, 428, L13
Narayan, R., & Yi, I. 1995, ApJ, 452, 710
Novikov, I. D., & Thorne, K. S. 1973, Black Holes (Les Astres Occlus) (New York: Gordon and Breach), 343
Parker, E. N. 1958, PhRv, 109, 1328
Parker, E. N. 1966, ApJ, 145, 811
Petrucci, P. O., Ursini, F., De Rosa, A., et al. 2018, A&A, 611, A59
Pessah, M. E., & Psaltis, D. 2005, ApJ, 628, 879
Piano, G., Tavani, M., Vittorini, V., et al. 2012, A&A, 545, A110
Pica, A. J., Smith, A. G., Webb, J. R., et al. 1988, AJ, 96, 1215
Pringle, J. E. 1981, ARA&A, 19, 137
Qiao, E., & Liu, B. F. 2017, MNRAS, 467, 898
Remillard, R. A., & McClintock, J. E. 2006, ARA&A, 44, 49
Romero, G. E., Torres, D. F., Kaufman Bernadó, M. M., & Mirabel, I. F. 2003, A&A, 410, L1
Rózanska, A. 1999, MNRAS, 308, 751
Rozanska, A., & Czerny, B. 1996, AcA, 46, 233
Różańska, A., & Czerny, B. 2000, MNRAS, 316, 473
Salvesen, G., Armitage, P. J., Simon, J. B., & Begelman, M. C. 2016a, MNRAS, 460, 3488
Salvesen, G., Simon, J. B., Armitage, P. J., & Begelman, M. C. 2016b, MNRAS, 457, 857
Sartori, L. F., Schawinski, K., Trakhtenbrot, B., et al. 2018, MNRAS Letters, 476, L34
Shakura, N. I., & Sunyaev, R. A. 1973, A&A, 24, 337
Shapiro, S. L., Lightman, A. P., & Eardley, D. M. 1976, ApJ, 204, 187
Simon, J. B., Beckwith, K., & Armitage, P. J. 2012, MNRAS, 422, 2685
Smak, J. 2000, NewAR, 44, 171
Stone, J. M., Hawley, J. H., Gammie, C. F., & Balbus, S. A. 1996, ApJ, 463, 656
Sorathia, K. A., Reynolds, C. S., Stone, J. M., & Beckwith, K. 2012, ApJ, 749, 189
Sunayev, R. A., & Titarchuk, L. G. 1980, A&A, 86, 121
Suzuki, T. K., & Inutsuka, S.-I. 2014, ApJ, 784, 121
Vallee, J. P. 1996, A&A, 308, 433
Van Eck, C. L., Brown, J. C., Stil, J. M., et al. 2011, ApJ, 728, 97
van Paradijs, J., & McClintock, J. E. 1994, A&A, 290, 133
van Paradijs, J., & McClintock, J. E. 1995, in X-Ray Binaries, ed. W. H. G. Lewin, J. van Paradijs, & E. P. J. van den Heuvel (Cambridge: Cambridge Univ. Press), 58
Warner, B. 2003, Cataclysmic Variable Stars (Cambridge: Cambridge Univ. Press)
Winters, W. F., Balbus, S. A., & Hawley, J. F. 2003, ApJ, 589, 543
Wojaczyński, R., Niedźwiecki, A., Xie, F.-G., & Szanecki, M. 2015, A&A, 584, A20
Yuan, F. 2001, MNRAS, 324, 119
Yuan, F., & Narayan, R. 2014, ARA&A, 52, 529
Zdziarski, A. A., Ghisellini, G., George, I. M., et al. 1990, ApJL, 363, LI
Zhu, Z., & Stone, J. M. 2018, ApJ, 857, 34